44th AIAA/ASME/SAE/ASEE Joint Propulsion Conference & Exhibit
21 - 23 July 2008, Hartford, CT

AIAA 2008-4965

Imaging Sensor for Chemical Species, Temperature and Pressure Measurements

Shin-Juh Chen[1], Joel A. Silver[2], Daniel J. Kane[3], and David S. Bomse[4]
Southwest Sciences, Inc., 1570 Pacheco Street, Suite E-11, Santa Fe, NM 87505

A compact, high speed, in-flight scramjet imaging sensor is being developed for the measurements of local temperatures, pressures and gas concentrations. This sensor is referred to as full laser absorption spectroscopic imager (*f*-LASIM). Its unique feature is a high speed imaging array detector that, when combined with laser diode wavelength modulation absorption spectroscopy (WMS) and custom electronics, provides an unprecedented combination of temporal and spatial resolution for real-time measurement of combustion gas properties. This paper discusses preliminary results that were obtained to demonstrate the feasibility of the lock-in imaging detector array to perform real-time, high speed, high sensitivity measurements relevant to scramjet engines including measurements of gas concentration, temperature and pressure with high spatial resolution even for weak absorbance levels. This sensor has application not only to scramjet development, but more broadly to all engine diagnostics and other systems where gas concentrations and flow properties need to be measured and understood.

Nomenclature

α	=	absorbance
b^0_j	=	broadening coefficient
β	=	modulation depth
d	=	characteristic length
$\Delta\nu_D$	=	Doppler half width at half maximum
$\Delta\nu_L$	=	Lorentzian line shape half width at half maximum
$\Delta\nu_V$	=	Voigt half width at half maximum
E_{rot}	=	rotational state energy
f	=	laser modulation frequency
g	=	line shape function
I_o	=	incident light intensity
I	=	transmitted light intensity
L	=	optical path length
M	=	molecular weight
m	=	modulation index
N	=	gas number density
n	=	detection harmonics
n_j	=	temperature coefficients
P	=	gas pressure
R	=	universal gas constant
S	=	line strength
T	=	gas temperature
t	=	time
T_0	=	reference gas temperature

[1] Senior Research Scientist, AIAA Member.
[2] Principal Research Scientist.
[3] Principal Research Scientist.
[4] Principal Research Scientist.

V = gas velocity
ν = laser wavelength
ν_0 = center laser wavelength
χ_j = mole fraction of species j

I. Introduction

DEVELOPMENT of scramjet engines for aerospace vehicles requires testing of engine components (e.g., inlet, isolator, combustor, nozzle, etc) in wind tunnels (free-jet or direct-connect) and, more importantly, in flight. These tests provide valuable information for developing a viable engine and means for deciphering some of the complexities inherent in such a system. The short flow residence time (milliseconds) inside the combustor poses a tremendous challenge to achieve appropriate mixing of fuel and air, and maintaining flame stability. Moreover, current wind tunnels cannot fully replicate the flow conditions expected to be encountered during flight or provide meaningful test times for current diagnostic tools. Yet, experimental data are crucial for validating current CFD models, and for developing new models for achieving high-fidelity simulations important to the scramjet engine designers.

During wind tunnel testing of isolator-combustor components, the inflow is usually uniform and does not reproduce the highly distorted flow profiles caused by oblique shocks generated in a typical scramjet inlet and interactions with the inlet boundary layer. Experimental modifications to these inflows are currently being made to realistically simulate typical distortions experienced in flight [1]. These distortions have a direct impact on the mass flux distribution at the isolator exit plane, affecting combustor performance and operation. Fuel injection flow rate and pattern must be adjusted to accommodate nonuniform velocity fields for optimum combustor performance. A diagnostic tool to image these inflow distortions non-intrusively during wind tunnel testing and in flight is needed. The imaging sensor could provide such measurement capability.

Wall cavities have been used successfully as flameholders inside combustors because they provide sufficient residence time for fuel and air to mix and burn, while generating low total pressure loss in comparison to bluff body flame stabilizers [2]. These flameholders provide a pilot light to spread hot combustion products into the main flow. Within the cavity, fuel injection is provided and a recirculation zone is formed. The boundary layer formed ahead of the cavity and the recirculation zone (subsonic) interact to form a shear layer that brings fresh oxidizer into and removes products from the cavity into the core airflow. However, several issues remain to be resolved regarding these cavity flameholders in terms of combustion efficiency and minimization of total pressure loss. Although extractive methods have been used to examine gas compositions inside the cavities [3-5], these methods cannot provide the spatial and temporal resolution that will be possible with the non-intrusive optical imaging diagnostic discussed here.

The expansion of the hot combustion products in the nozzle section of the scramjet engine generates the thrust for the vehicle. Knowing the distribution of the combustion species and temperature along and across the nozzle section, and the back pressure is important for assessing the overall engine performance during test flights. The imaging sensor discussed here has the potential to provide these essential flow properties as well.

The imaging technology was successfully demonstrated in our laboratory. Custom signal processing electronics combined with a custom linear array detector provided high-speed and high-sensitivity gas measurement capabilities. We demonstrated spectroscopic methods for non-invasive gas temperature and pressure measurements.

II. Methods

A. Imaging Lock-In Detector Array (LIDA)

Most modern imaging devices rely on charge integration in charge-coupled devices (CCD) or active pixel technologies. In these devices, a two-dimensional array of photodiodes acts as the light sensitive element. The charge generated by light hitting each photodiode is accumulated in a capacitor (*i.e.*, one capacitor per photodiode).

In the case of a CCD, each capacitor is coupled to its neighbor in a way that allows its charge to be moved to its neighbor via a clock signal. Thus, the accumulated charges can be clocked out and individually read by a combination of an amplifier and analog-to-digital converter. These serial readouts are slow. Alternatively, active pixel sensors, commonly known as the CMOS sensors, consist of three transistors and a photodetector. Pixels are arrayed in two dimensions, with some circuitry shared by pixels in adjacent rows and columns. While active pixel sensors do have some advantages over CCD sensors and have a source follower amplifier built into each pixel, the

amplifier only provides a small amount of current gain. Additional gain must be provided at each column or row. These CCD and CMOS sensors are not suitable for high speed imaging.

Consequently, we developed a parallel imaging solution that uses an array of individually addressable photodiodes. A schematic diagram of the detector array is shown in Fig. 1. Our first generation detector has 76 silicon photodiodes in one row that are simultaneously sampled at 96 kHz. The output from each photodiode is amplified using a transimpedance amplifier, conditioned with a programmable gain amplifier, and digitized using a 24-bit analog to digital converter with a dynamic range of over 100 dB. The digital output streams to a field programmable gate array (FPGA) for preprocessing and buffering before being transferred to a computer via a digital frame grabber. Even though we are using only 76 photodiodes for each array, the data acquisition electronics and software are efficiently scalable in parallel. Two multiple demodulating arrays can be used with each frame grabber, and several frame grabbers can be placed into a computer, readily permitting images of 456 or more pixels in linear or rectangular arrays. Currently, the FPGA is programmed to demodulate and then low pass filter the A/D output. However, the FPGA could be programmed with virtually any other algorithm such as a high pass filter; demodulation at multiple harmonics, etc.

Demodulation at multiple harmonics is particularly interesting. Measurements demonstrated gas pressure determination based on the ratios of spectral intensities for WMS spectra acquired at multiple harmonics. For the imaging array, multiple harmonic data are nearly "free." The information is contained in the digitized photodiode signal, and is easily extracted using a simple vector dot product or Fast Fourier Transform (FFT).

The currently available device provides a good match of speed with desired imaging resolution. Detector elements are spaced at ~0.3 mm (with a height of 3.0 mm), but with appropriate optics can readily image widths of 1 – 20 cm. Given a "typical" gas velocity as high as $V = 1000$ m/s and a desired spatial resolution of $d = 3$ mm, the commensurate bandwidth would be $V/d \approx 33$ kHz. Currently, the maximum sampling rate from the A/D's is 96 kHz (hardware limitation). The imager runs continuously, so as to be able to capture both short and long term flow and combustion instabilities, but the actual bandwidth is the laser sweep rate because one spectrum equals one measurement. For wavelength modulation spectroscopy, we need to modulate the laser current at about 20 kHz, and detect at 40 kHz ($2f$). We typically use 100 points per wavelength scan to resolve the absorption features. This means that the laser current scan rate is 200 Hz and defines the actual measurement speed. This rate can be increased by several means;, for example, (1) reduce the number of points per wavelength scan (using just 50 points will give 400 Hz measurement rate for WMS), (2) sit at the peak of the absorption line (10's kHz measurement rate can be readily achieved), and (3) conduct direct absorption measurements (up to 5 kHz measurement rate with 100 points per waveform). To our knowledge, no other imaging sensor even comes within an order of magnitude of this capability.

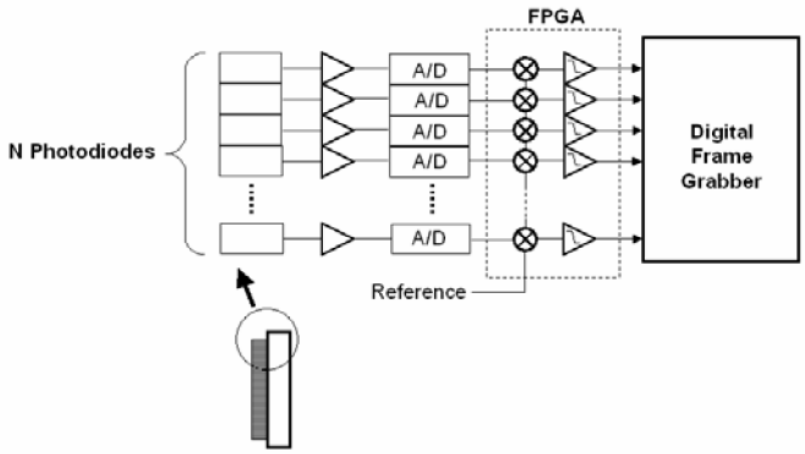

Figure 1. Schematic diagram of imaging sensor. Signal from each photodiode is sent to a transimpedance amplifier, programmable gain amplifier, 24-bit A/D converter, field programmable gate array (FPGA), and computer via a digital frame grabber.

B. WMS Spectral Measurements and Spectroscopy

The greatest advantage of optical absorption spectroscopy is that the resulting signal is linear in concentration of the absorbing species and is quantitative. The observed signal is simply proportional to the absorbance described by Beer's law where the fractional intensity of light absorbed by a gas sample at wavelength ν is

$$\frac{\Delta I}{I_0} = \frac{I_0(\nu) - I(\nu)}{I_0(\nu)} = \alpha(\nu) \quad , \tag{1}$$

where I_o is the incident light intensity on the gas sample and I is the intensity reaching the detector.

The absorbance line shape α(υ) is given by the line strength S, the normalized line shape function g(υ) (dependent on temperature, pressure and the mole fractions of each gas χ_i), the gas number density N and the absorption path length L. The line strength is weakly dependent on temperature, but independent of pressure. For absorption coefficient α values below about 0.1, Eqn. (1) can be expanded and rearranged to provide the mole fraction or mixing ratio χ for the measured sample,

$$\chi = \frac{N}{N_{total}} = \frac{\alpha(\nu)}{S(T) g(\nu) L} \cdot \frac{RT}{P} \quad , \tag{2}$$

where R is the gas constant.

The normalized line shape g(ν) in Eqn (2) is best represented by a Voigt function, which is a convolution of the Lorentzian line shape (homogeneous broadening) and a pressure-independent Doppler (Gaussian) line shape arising from inhomogeneous broadening [6],

$$\begin{aligned}
g_{Doppler} &= \frac{1}{\Delta\nu_D}\left(\frac{\ln 2}{\pi}\right) \exp\left[-\ln 2\left(\frac{\nu-\nu_0}{\Delta\nu_D}\right)^2\right] \quad , \\
with \quad \Delta\nu_D &= 3.571\times10^{-7}\ \nu_0\sqrt{T/M} \quad (HWHM), \\
g_{Lorentz} &= \frac{1}{\pi}\frac{1}{\left[\left((\nu-\nu_0)/\Delta\nu_L\right)^2+1\right]} \quad , \\
with \quad \Delta\nu_L &= P\sum_j b_j^0\left(\frac{T_0}{T}\right)^{n_j}\chi_j \quad (HWHM), \\
g_{Voigt} &= \int g_{Doppler}\, g_{Lorentz}\, d\nu \ ,
\end{aligned} \tag{3}$$

where ν_0 the center frequency of the transition, and M the molecular weight in amu. The Doppler half width at half maximum (HWHM), $\Delta\nu_D$, is proportional to the square root of temperature and independent of pressure. By contrast, the Lorentzian line shape half width $\Delta\nu_L$ is linearly proportional to pressure and the broadening coefficients b_j of each gas component j in the mixture, weighted by the corresponding mole fraction χ_j of that component. In addition, each broadening coefficient is weakly dependent on temperature, where the reference value b^0_j is defined at T_0 = 296 K and the temperature coefficient n_j typically ranges from 0.5 to 1.0 [7].

The drawback of direct absorption is that it is limited in sensitivity because it is difficult to measure the small difference between two large values (I and I_o; Eqn. 1). Wavelength modulation spectroscopy allows measurement of weak optical absorbances by shifting the detection band to high frequencies where laser excess ($1/f$) noise is unimportant and can achieve fractional absorption sensitivities to near the shot-noise limit (~10^{-7}) [8,9]. To implement WMS, a small sinusoidal modulation at frequency f is superimposed on the diode laser injection current which produces a modulation of the laser wavelength, since wavelength is tuned by changing the current. The amplitude of the current modulation is chosen so that the induced wavelength modulation is comparable to the width

of the spectral feature under study. As illustrated in Fig. 2, absorption by the target gas converts the laser wavelength modulation β to an amplitude modulation (green region on top curve) that induces ac components in the detector photocurrent. Phase-sensitive electronics are then used to demodulate the detector photo-current at a selected harmonic, nf (typically, $n = 2$). By implementing this technique at sufficiently high frequencies (10's of kHz or greater), $1/f$ laser noise is minimal and detector-limited sensitivity can be achieved. In the imaging array detector the demodulation is performed digitally, as is done in high quality commercial lock-in amplifiers (phase sensitive detectors).

The extent of modulation (modulation depth) is represented by a dimensionless number m that is the ratio of the maximum laser wavelength excursion about the initial wavelength divided by the Voigt half width (HWHM) $\Delta\nu_v$. These quantities are typically expressed in wavenumbers with β being the modulation-induced wavelength excursion. Thus $m = \beta/\Delta\nu_v$ and the instantaneous wavelength of the laser is

$$\nu(t) = \nu_i + \beta\sin(\omega t)\,, \tag{4}$$

where ν_i is the laser wavelength at ramp injection current i, t is the time, and $\omega = 2\pi f$ is the modulation frequency. As discussed below, the optimum value of m varies with detection harmonic, but for the typical $n = 2$ system, the best modulation depths are about 2.2.

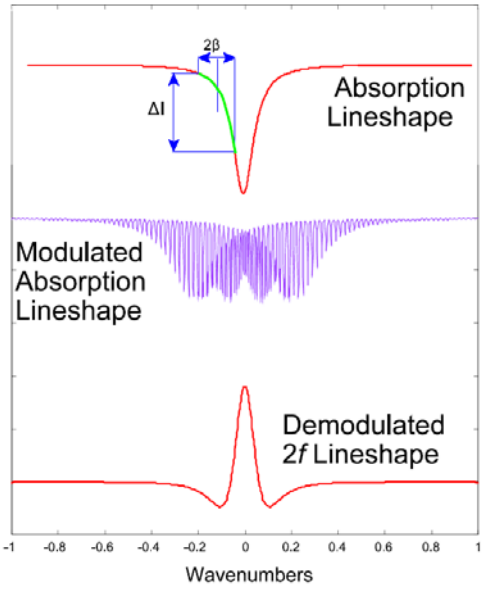

Figure 2. Generation of wavelength modulation spectroscopy (WMS) spectrum from transmission line shape.

Our field measurements using WMS routinely maintain minimum detection absorbances of better than 10^{-5} (1 Hz bandwidth) for extended (many month) operation [10-12] with a detection limit of better than 3×10^{-6} for short durations. Although the (detector and laser-induced shot) noise limits for these systems are typically below the 3×10^{-7} absorbance levels, the limiting factor in these measurements is most often interference fringes (etalons) induced by unwanted back-reflections in the optical paths. While the signal-to-noise ratio (SNR) improves as the averaging time increases ($t^{½}$ dependence) for the noise components, etalons look like absorbances and their magnitude is independent of t. Thus for high bandwidth applications, noise components may dominate the etalon effects. For example, if the etalons are equivalent in magnitude to an absorbance of 1×10^{-5} and the 1 Hz shot/detector noise is 3×10^{-6} (assumed higher than usual here because of the harsh flame environment), at a detection bandwidth of 1 kHz, the minimum detectable absorbance would be $\sim 1\times10^{-4}$, so that the noise exceeds the etalon effects. Given that we expect absorbance levels in scramjet wind tunnels and aircraft measurements to range from 5×10^{-3} to 1×10^{-1}, excellent signal-to-noise ratios can be expected, even accounting for degradation of sensitivity due to the harsh environment.

Because this first version of the imaging lock-in sensor has a silicon photodiode array, it restricts the gases we can reasonably measure to oxygen (760 nm) or water vapor (940 nm). Since water is a ubiquitous product of any hydrocarbon combustion process (including H_2-fueled engines), it is an ideal candidate for monitoring combustion temperatures, pressures and gas concentration. The observed absorption spectra are weighted averages of spectral data along the line-of-sight of the field-of-view of the probe, which can be analyzed using the Air Force HITRAN database [7] and/or calibrations performed in the laboratory.

C. Measuring Gas Properties - Concentration

Both water vapor and oxygen measurements were conducted using our high speed imaging array. Water vapor was initially measured using a diode laser operating near 947 nm in both room air and in a methane-air diffusion flame (Wolfhard-Parker burner). This wavelength is not optimal for determination of temperature, so a suitable laser will be used in future work. Oxygen measurements were conducted using a 760 nm vertical cavity surface emitting laser (VCSEL). Tuning rates (cm^{-1}/mA) for the laser ramp and modulation were calibrated using a solid etalon having a free spectral range of 0.2265 cm^{-1}.

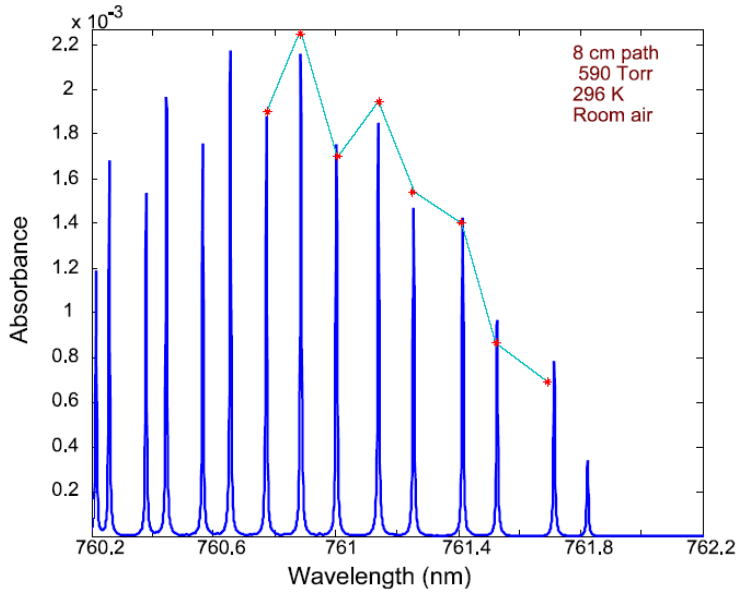

Figure 3. Measured and computed oxygen spectrum. Red markers denote measured positions and absorbances of sample.

For the oxygen measurements, the spectrum was scanned over a wide wavelength range to characterize the laser used. Figure 3 shows the predicted HITRAN spectrum of oxygen (solid blue curves), along with observed absorbances and spectral locations from our scan (observed peaks at red crosses). The experimental data match up well to HITRAN data and permit us to determine the tuning characteristics of the laser. For the temperature and spatial examination measurements using the imaging array, we used the R^5R^5 line at 13136.218 cm^{-1} (761.3 nm).

D. Measuring Gas Properties - Temperature

The temperature is found by measuring the absorbance ratio of two lines having different rotational ground state energies. Figure 4 illustrates the dependence on temperature of two spectral lines of water vapor near 950 nm. Combining Eqns. (1) and (4), with knowledge of the temperature dependence of S,

$$\frac{\alpha_1(\nu)}{\alpha_2(\nu)} = \frac{g_1(\nu)S_1(T_0)}{g_2(\nu)S_2(T_0)} \cdot \exp\left\{\frac{\{E_{rot,1} - E_{rot,2}\}}{k}\left(\frac{1}{T} - \frac{1}{T_0}\right)\right\}. \quad \textbf{(5)}$$

From this equation (or equivalently, a measured calibration curve), the observed line shape ratio dependence on temperature is found by fitting the two line shapes using a singular valued decomposition (SVD) analysis. For the gases and temperatures of interest, this dependence is a monotonic function as illustrated in Fig. 5 for water vapor. For this example, a ratio measured with 1% accuracy corresponds to a temperature uncertainty of only ± 25 K. Once temperature is established, the mole fraction is readily found using Eqn. (2). This approach has been demonstrated by a number of researchers as a means to obtain temperature [13-15]; however, the imaging sensor will accomplish this simultaneously for all 76 spatial channels.

For oxygen, we selected the adjacent R^9R^9/R^7Q^8 line pair to determine temperature. The sensitivity to these and other line pair ratios is shown in Fig. 6. Note that for alternating adjacent line pairs,

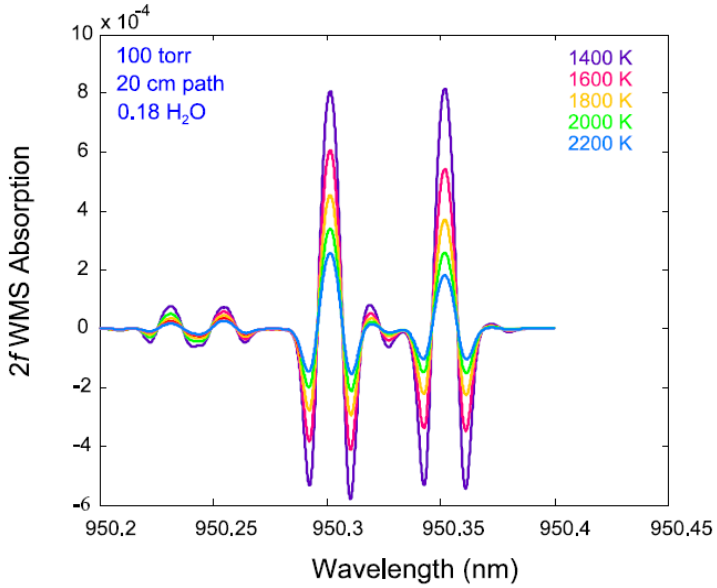

Figure 4. Potential line pair of water near 950 nm used for temperature and concentration measurements.

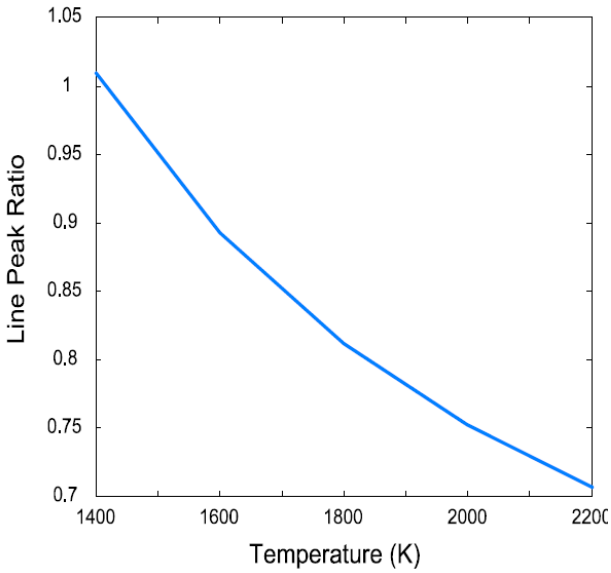

Figure 5. Line pair peak height dependence as a function of temperature.

the RQ/RR line ratios are independent of temperature because they both originate from the same rotational ground state and thus have the same temperature dependence. New lasers selected specifically for optimal wavelengths for both oxygen and water vapor measurements will be used in future studies. The sensitivity for measuring temperature should be improved by at least a factor of two.

E. Measuring Gas Properties - Pressure

The width of an absorption line is a strong measure of pressure. For pressures relevant to the scramjet, the line shape is described by the Voigt profile. Ambient pressure can be directly found from the observed line width using direct absorption, which requires absorbances above 1%. However, the expected absorbance levels for oxygen in the inlet or products in the combustor most likely will be much smaller than 1%, so that a direct measurement of the line shape (pressure) is precluded. Unfortunately, derivative methods such as WMS can't readily provide the width directly from the line shape, as the WMS shape is relatively insensitive to pressure and more dependent on the modulation depth. Simulations confirmed this fact. Assuming that one knows neither the absolute concentration nor pressure, one finds that the off-axis terms in the correlation matrix in a non-linear least squares fit are large, so that the fit can not readily separate the effect of pressure from concentration on the overall line shape.

However, we have examined three alternative approaches to determine the pressure using the more sensitive WMS spectra. The first approach uses the 2*f* trough-trough spacing, which is a near-linear function of the modulation index *m* (and thus the pressure). A second approach uses the design of Goldstein [16], where the shape of the peak-peak signal versus modulation depth value is a function of the half width or pressure. The drawback of this approach is that one must make multiple spectral measurements over a range of modulation depths to find the half width.

A third method to determine the line width using WMS by comparing the peak signal value at different detection harmonics [17] is available. With this approach, one can simultaneously demodulate the signal at not only the second harmonic, but also the first, third, fourth, etc., as permitted by the electronics. Using the already measured temperature (see above), the pressure is retrieved using the known spectral parameters with Eqn. 3.

An important consideration for all of these approaches is the selection of the specific absorption line(s) to monitor. When the rotational state energy $E_{rot} \approx kT$, the observed peak height is quite insensitive to changes in temperature, so that these lines are best for finding the pressure. For temperature sensitivity, one

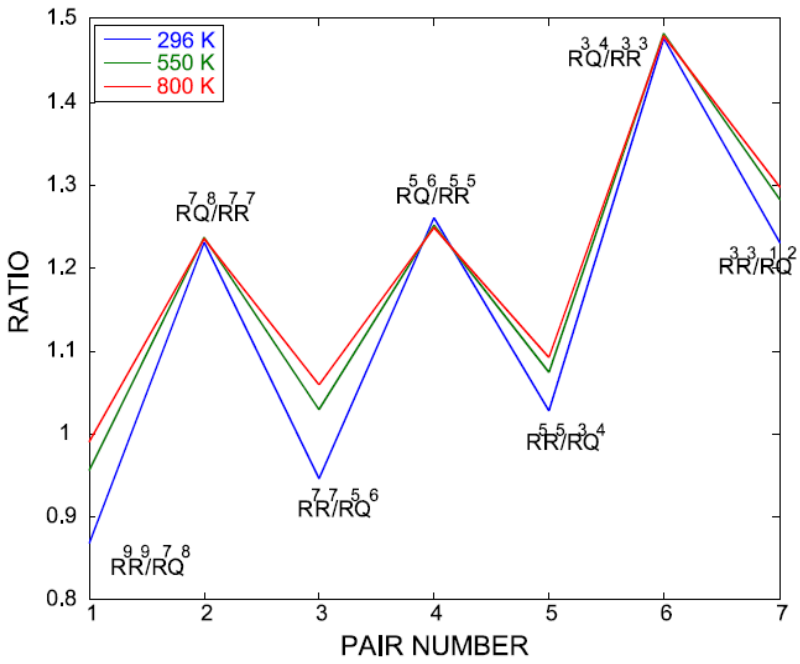

Figure 6. Temperature dependence of line pair ratios.

generally selects lines that have widely differing ground rotational energy levels (Eqn. 5).

III. Results and Discussion

A. Data Collection

The lock-in detector array (LIDA) obtained nearly shot-noise-limited detection of oxygen at atmospheric pressure with excellent time response. A software timing issue – a problem synchronizing the start of each laser wavelength scan with the frame grabber data collection – prevented real time data imaging. Instead, data were saved in "chunks" of bitmap files containing 4096 lines of data. The maximum A/D sample rate was 96 kHz; each bitmap contained 42.7 ms of continuous data providing ample time to demonstrate the unique capabilities of our technology. The data were read using MATLAB as a matrix with 4090 rows × 80 columns; 76 columns contained pixel data while the other 4 columns contained line counts and framing marks.

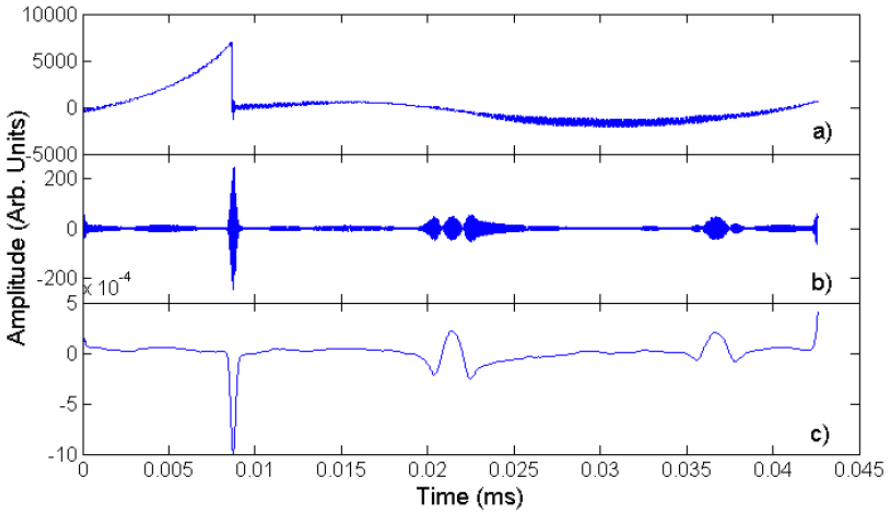

Figure 7. Steps required to process the data from LIDA for imaging wavelength modulation spectroscopy. (a) shows the raw data from LIDA; (b) shows the in-phase 2*f* component of the signal only; (c) is the demodulated 2*f* showing oxygen absorption features at 0.21 and 0.37 msec.

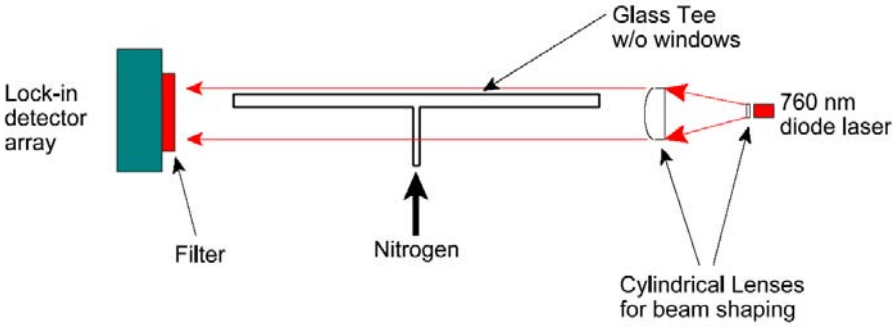

Figure 8. Schematic of the experimental apparatus used to test resolution and measurement of gas profiles. Nitrogen gas is continuously flown into the glass tee.

All the pixel data were digitally processed in MATLAB. Each column was Fourier transformed, and windowed around the second harmonic of the diode laser modulation frequency. The windowed data were then inverse Fourier transformed, multiplied by a phase-selected sine wave at the second harmonic of the laser modulation frequency, and low pass filtered to extract in-phase and out-of-phase 2*f* absorption spectra. To normalize the pixel response and to reduce pixel-to-pixel fluctuations, the 2*f* output from each pixel was normalized by the root-mean-sum of each pixel's raw data. Figure 7 illustrates the waveforms during the various processing steps. Spectra at other harmonics can also be extracted from these data.

Figure 8 is a schematic diagram illustrating how the 2*f* performance of the LIDA was tested. Nitrogen flowed into the stem of a glass tee (30 cm long × 6.7 mm I.D.). The top of the tee was placed into the beam between the line shaping optics and the LIDA. The remaining open air path is approximately 26 cm long. Thus, when pure nitrogen is flowed through the tube, a depletion of about 53% is expected.

Figure 9 shows a single scan of oxygen absorption when pure nitrogen is flowing in the tube. The region from 0 to 6 mm clearly shows an oxygen depletion of 50 - 60 % as compared to the region from −12 mm to −3 mm. Upward peaks at −4 and +6 mm are due to the tube shadow on the detector. The region from 7 to 13 mm had insufficient laser power to provide a reliable measurement.

Pixel-to-pixel variation is mostly due to differing absolute pixel responsivities (which can be calibrated out, as done in all camera systems), not to noise in the measurements. Indeed, by examining the fluctuations in time of individual pixels in the region between −12 mm and −3 mm, we can determine that the fluctuation in the percent change in oxygen absorption to be about 10 %. Over a 56 cm path, this corresponds to a fluctuation of $5 - 6 \times 10^{-4}$ in total absorbance. Because only peak-to-trough values were used (fitting the whole line shape would improve the results), the bandwidth of the measurement is about 300 Hz, which yields a noise value of $3 \times 10^{-5}/\sqrt{\text{Hz}}$ for the oxygen measurement.

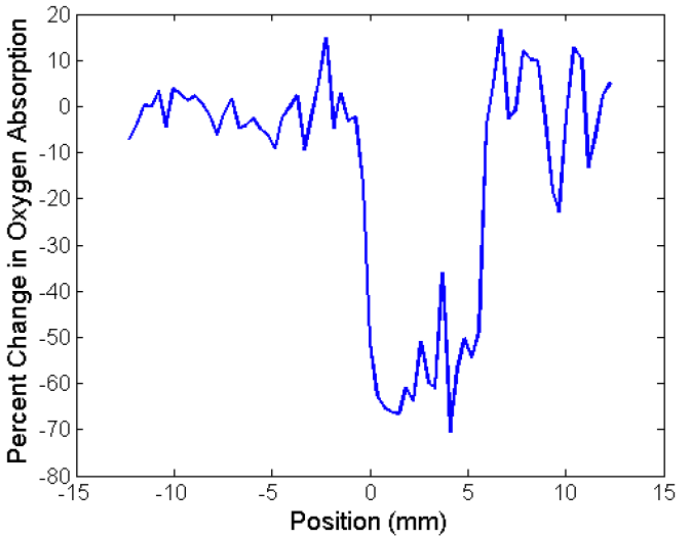

Figure 9. Depletion of oxygen as seen by the imaging array at the exit of the glass tube. Nitrogen gas is flown into the tube. Position between 0 and 6 mm is the glass tube.

As mentioned earlier, the detector board was optimized for a different application where much lower levels of light were expected. The laser output had to be attenuated in order to keep the transimpedance stage of the amplifier from saturating. Consequently, the noise value can be improved by approximately a factor of 3 to 5 by optimizing the gain of the transimpedance amplifiers for incident laser power.

B. Sensitivity, Spatial Resolution, Time Response, and Dynamic Range

LIDA was also evaluated using water vapor in room air as the absorbing gas, Fig. 10. The laser beam is formed into a thin sheet (~1 mm high × 25 mm wide) using a pair of cylindrical lenses. This sheet of light traverses the sample region (open air, flame or sample tubes) and is then re-imaged onto the array using a pair of aspheric lenses. For the initial characterization study, a rotating chopper blade was inserted in the path near the laser, and a chopping speed of 1 kHz used to determine the time response. The location of the laser sheet is illustrated by the red band in the figure. A 947 nm vertical cavity surface emitting diode laser (220 μW) is used in these measurements.

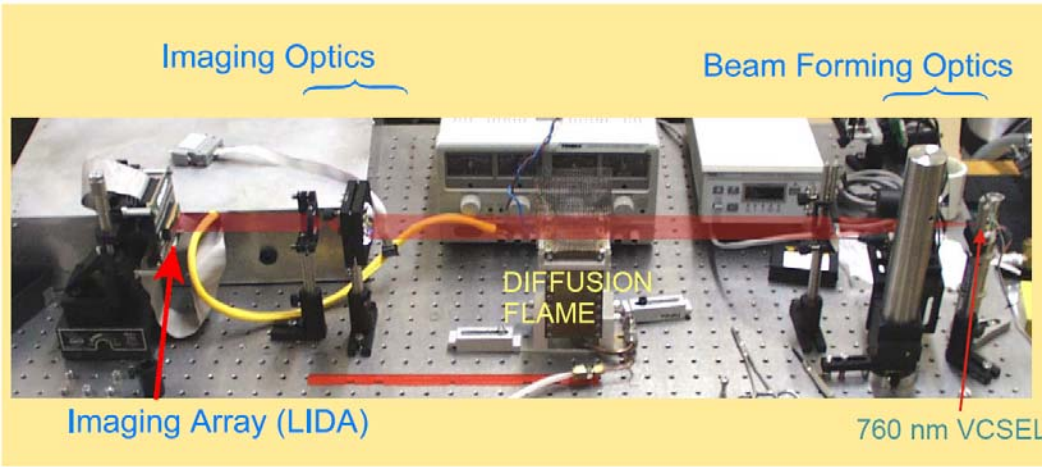

Figure 10. Test setup for testing the imaging sensor.

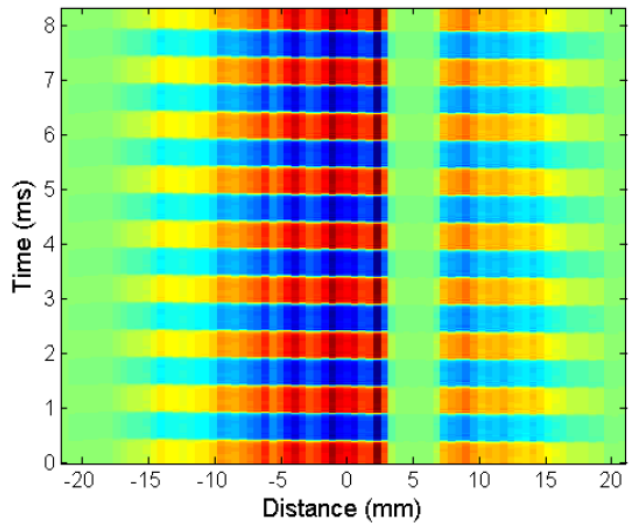

Figure 11. Intensity versus distance and time of chopped laser beam as imaged by LIDA.

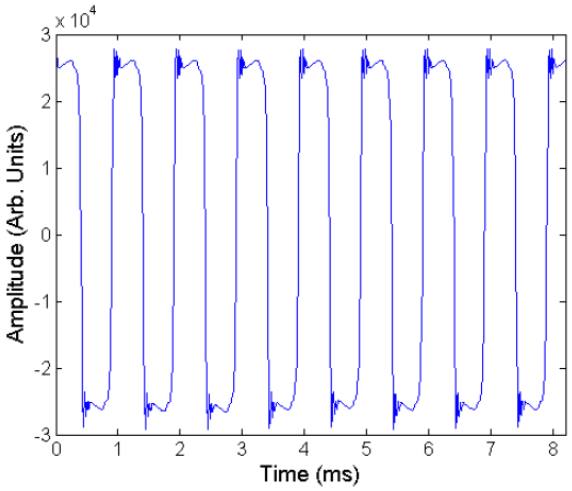

Figure 12. The time history of a single pixel from the image in Fig. 11.

this device.

Figure 12 is a plot of the time response of a single pixel from the image shown in Fig. 11 over an 8 ms time period. The laser is mechanically chopped at a frequency of 1 kHz. The detailed rise time, Fig. 13, is the time for the chopper to cut across the beam. The chopping edge was traveling at 1200 cm/sec. The blades traveled about 0.660 mm within the rise time of the signal, which is on the order of the physical height of the laser beam and the resolution of the detector array. Therefore, the time response of each pixel is better than 0.055 ms.

Two critical specifications of the lock-in detector array (LIDA) are the spatial and time resolutions. Spatial resolution determines the minimum size that can be imaged. Time resolution must be sufficient to differentiate between events of interest.

The spatial resolution is a function of the cross-talk between pixels, the pixel size, and the optical system used for imaging. Because each pixel is electronically independent, no cross-talk between the pixels is expected, and none was observed. (Tiny amounts of cross-talk caused by current leakage will be overwhelmed by diffraction effects in the optical imaging system.) Figure 11 shows an image of intensity vs. time and distance for an 8 ms block of data from the LIDA as the laser was being mechanically chopped at 1 kHz. An obstruction, that is 3 to 4 mm wide, was placed in the beam in the region from 3 to 7 mm. The edges are very sharp–within one pixel.

Each horizontal bar is comprised of about 100 measurements in time (96 kHz into each bin; vertical axis), and corresponds to the alternating beam open and blocked positions of the chopper. The false color image records red as full intensity and blue as zero, due to ac coupling. The edges where no light falls and the blocked stripe region are green (also zero, but in a dc sense).

In the absence of cross-talk, the ultimate spatial resolution is determined by a combination of the pixel size (pitch), the number of pixels, and the optical system. The Hamamatsu S3954 photodiode array used in the LIDA has 76 photodiodes that have a horizontal pitch of 0.343 mm and a vertical size of 3.175 mm. Optical system design will determine the ultimate trade-off between image size and resolution. So, the achievable spatial resolution is actually about 350 microns using

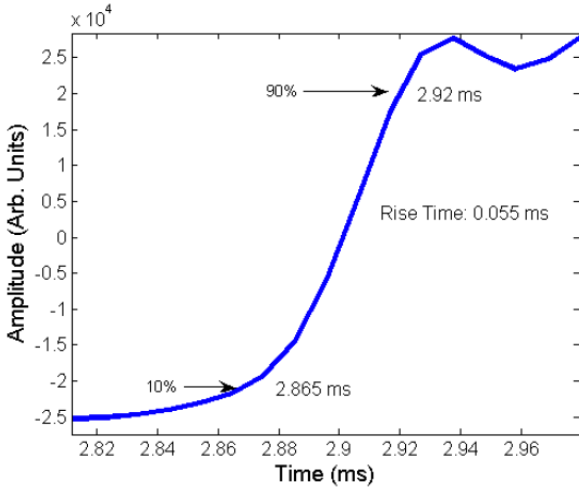

Figure 13. A section from the plot shown in Fig. 12 at 2.9 ms. The rise time is 0.055 ms.

The power spectrum, dynamic range, saturation power and minimum power of the imaging sensor were obtained using the oxygen VCSEL. Figure 14 shows a plot of the power spectrum on the array detector of two pixels, one where light intensity is large (2 mm) and one where it is low (−21 mm). In the upper trace (blue, at 2 mm), the maximum laser power is about 0 dB, and the power spectrum falls off to −80 dB at the Nyquist frequency. The spikes at all frequencies correspond to the Fourier transform of the chopped square wave (odd harmonics separated by 2 kHz). The lower trace (red, at −21 mm) shows very weak signals (array end point) where the power spectrum reaches the detector limit noise floor of about −115 dB. The dynamic range at a 96 kHz sample rate is better than 100 dB! The saturation power is 7.5 μW and the minimum power is less than 110 pW.

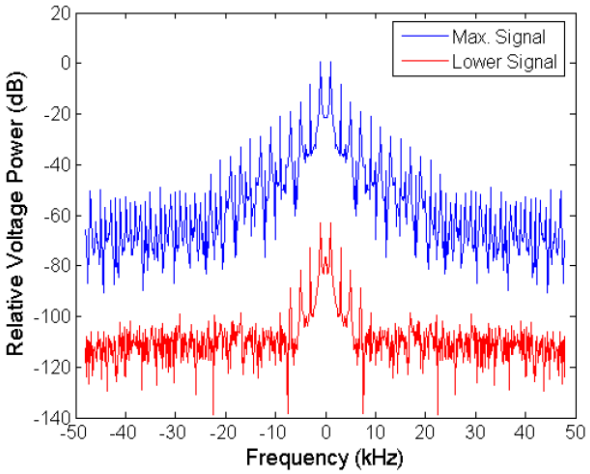

Figure 14. Plot showing the power spectrum of two pixels at about 2 mm (blue) and −21 mm (red) on the array detector.

C. Concentration Measurements

Since this array was originally designed for another application, we had to attenuate the laser intensity to prevent detector saturation. This in turn, limits the WMS detectability. In future work, we will replace the 76 transimpedance resistors with values appropriate to this application. Nevertheless, both water vapor and oxygen in ambient air can be measured with extremely good signal-to-noise ratio using the linear array detector with wavelength modulation absorption spectroscopy. For the water measurements, the laser was modulated at 15 kHz with 2*f* detection at 30 kHz. A sample water 2*f* spectrum collected by detector element No. 40 is shown in Figure 15. The spectrum was obtained with a laser scan rate of 55 Hz and 1750 points per spectrum.

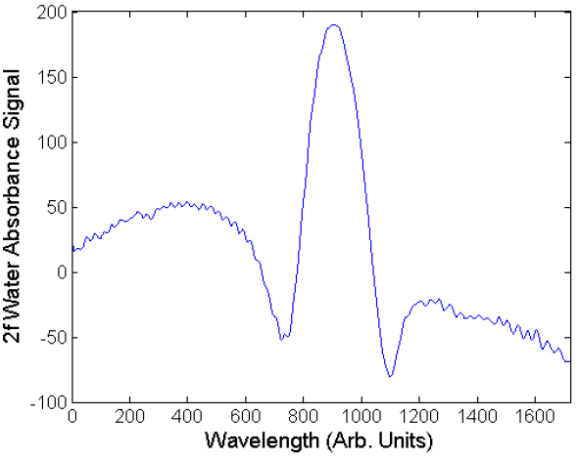

Figure 15. Sample water vapor 2*f* spectrum collected by detector element No. 40.

Preliminary oxygen measurements across the methane diffusion flame (using a Wolfhard-Parker burner) were obtained. The laser was modulated at 10 kHz, with 2*f* detection at 20 kHz. Figure 16 shows a sample oxygen 2*f* spectrum collected by detector element No. 40. Again, there is no time-averaging. This is single-shot data. All 76 elements of the array detector collect the oxygen spectra simultaneously. The laser was scanned at a rate of 28 Hz using 3400 points per spectrum.

Note that these spectra are single scans with no averaging and exhibit excellent signal-to-noise ratios. As discussed earlier, fixing the transimpedance gain values will actually improve the sensitivity by a factor of 3 to 5. Each of the 76 elements of the array detector collects a gas spectrum simultaneously.

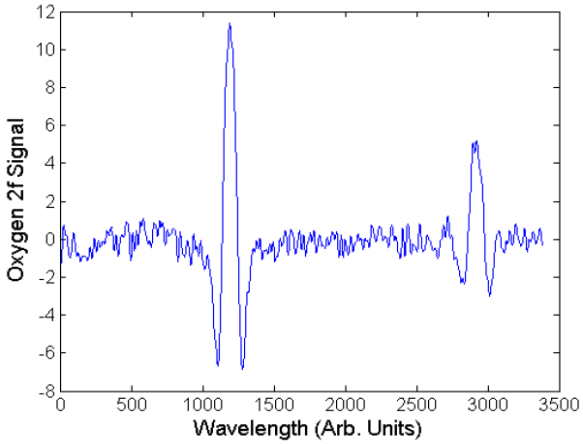

Figure 16. Sample oxygen 2*f* spectra collected by detector element No. 40.

D. Temperature Measurements

We used the R^9R^9, R^7Q^8 line pair of oxygen absorption line near 13144 cm^{-1} for this part of the

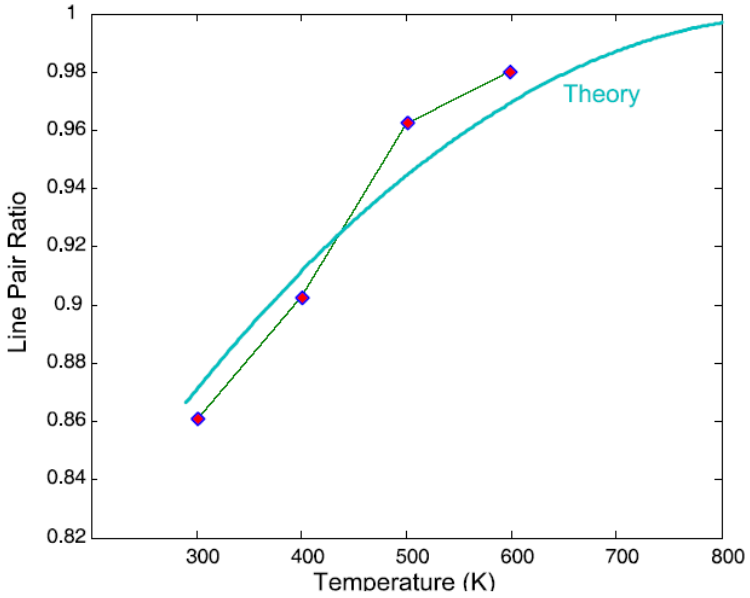

Figure 17. Temperature determined from line pair ratios using oxygen spectra. Solid curve is computed results. Symbols are experimental data.

study. Both a Wolfhard-Parker burner and Lindburgh furnace (capable of operation to 1370 K) were used to test for temperature measurements. We looked mostly at temperatures between 300 and 800 K in the furnace.

Preliminary results for these measurements are shown in Fig. 17. The temperatures inferred from the peak ratios are accurate to about ± 25 K. The spectra are noisier (Fig. 16) than will ultimately be observed once the gain and optimal wavelength issues are addressed. Nevertheless, we demonstrated successfully the capability of the imaging array for temperature measurements.

E. Pressure Measurements

Pressure can be determined using four different approaches: (1) direct fit of 2*f* WMS signals, (2) *m*-dependent curve fits, (3) trough-trough separations, and (4) harmonic ratio measurements. The key to measuring pressure is to select an approach that is unaffected by other parameters also being measured. For example, we always assume that the gas concentration is a measured parameter, so that peak heights alone more likely reflect the concentration than pressure. Thus it appears, to first order, that a method which does not depend solely on a single peak height measurement will aid in measuring pressure.

We used the R^7R^7 oxygen absorption line at 13,140.57 cm^{-1} in room air. Pressures were varied from 25 to 760 torr at room temperature for modulation depths ranging from 0.019 to 0.35 cm^{-1} for samples of 75% O_2 in N_2 in a 98 cm long gas-tight cell. Laser output, collimated by an aspheric lens, was directed through the cell and onto a 1 cm diameter Si photodiode. Output from the photodiode was input to a 1 MHz bandwidth current-to-voltage preamplifier set to 500 μA/V which, in turn, was connected to a lock-in amplifier (Stanford Research SR830). The preamplifier output was separately low-pass filtered (300 Hz, unity gain) and then digitized to provide a measurement of the laser intensity I_o at the detector. The cell was equipped with uncoated, BK-7 (Pyrex) windows hermetically sealed to a standard KF-40 flange. Gas pressures were monitored with an MKS Baratron (1000 torr head) and held stable to ±0.2 torr during each set of measurements. The O_2 concentration in the mixture was certified by the vendor (Matheson) to be 75.10%.

For each gas sample pressure, spectra were acquired as a function of modulation depth at 6 detection harmonics: 1*f* through 6*f*. The modulation frequency was 13.4 kHz. This is lower than is typical for wavelength modulation spectroscopy, but allowed us to detect up to 6th harmonic while staying within the 100 kHz limit of the lock-in amplifier. Each spectrum is a 256-step scan obtained by stepping the voltage output of a digital-to-analog converter that is part of the locking amplifier and using the voltage to program the laser controller driver current. This voltage was combined with the sine wave, also generated by the lock-in amplifier, using a summing amplifier, before being applied to the laser controller.

The laser wavelength scan range and linearity were measured by putting a solid etalon, 0.2265 cm^{-1} free spectral range into the optical path. Scans were observed to be highly linear and the etalon data match the wavelength scan range determined by increasing the current scan to also encompass an adjacent O_2 absorption line. Thus, the WMS spectra could be used without correction to determine line shape variations with pressure and modulation depth.

As discussed earlier, non-linear least squares fits to the observed line shapes did not do very well in distinguishing pressure, for the reasons discussed above. The approach of Goldstein utilizes a plot of peak-trough heights as a function of *m*. Each curve has a different shape for differing pressures, where these curves are normalized to their peak intensity. By measuring this curve for a variety of modulation depths, one could infer the Voigt half width corresponding to this curve, and hence the pressure (Eq. 3). Family of curves for $n = 2$ WMS detection as a function of *m* for different pressures were obtained. While differing curves could be distinguished,

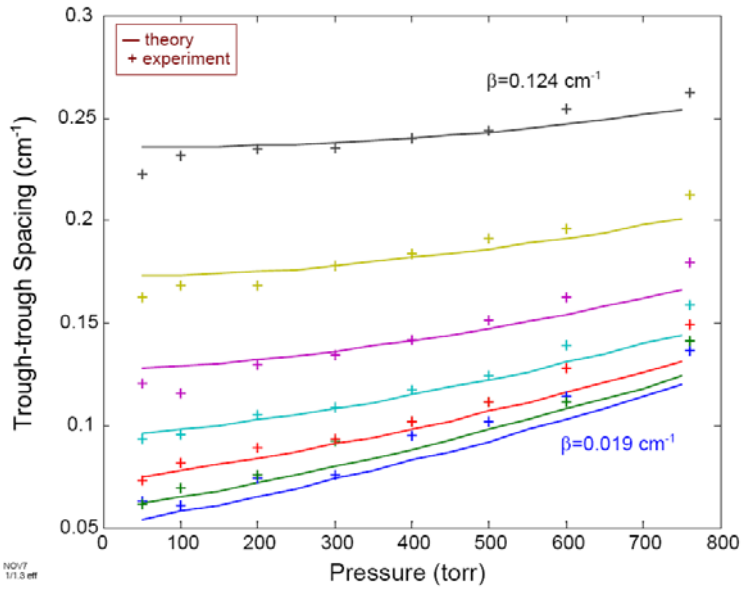

Figure 18. Trough separations as function of pressures for range of modulation depths.

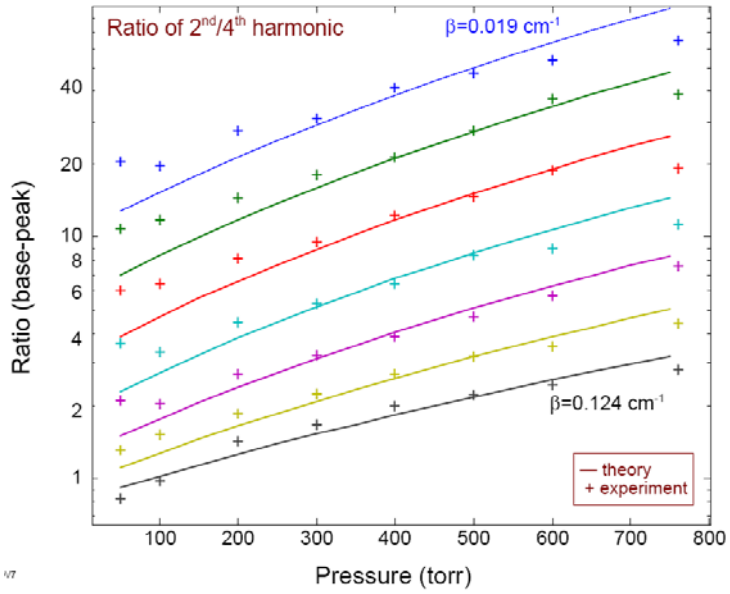

Figure 19. Peak height ratios for *n*=2 to *n*=4 WMS signals as a function of pressure for various modulation depths

their separation was not particularly large. This approach works reasonably well in the laboratory, but it is impractical for a real-time diagnostic because multiple spectral measurements over a range of modulation depths would be needed for each pressure determination.

The last two approaches for determining pressure can be made with a single spectral measurement. We computed trough–trough wavelength separation (or peak–trough for odd harmonics) as a function of modulation depth β for a series of pressures ranging from 50 to 760 torr. In general, the odd harmonic family of curves intersects at lower modulation depths. The even harmonics are more widely spaced at lower modulation depths and converge at higher values. The Voigt half widths range from 0.019 to 0.035 cm^{-1} over the pressure range shown. Modulation depths that would provide reasonably large signal levels are in the range of 0.03 to 0.1 cm^{-1}. Thus, the $n = 2$ system appears ideal for distinguishing the ambient pressure based on the trough-trough separation of the $2f$ spectra. Figure 18 compares measured and computed trough-trough separations for $n = 2$ in a region of lower modulation depths for a number of different pressures. The data points are color-coded to match the respective theoretical pressure curves. When the signals are noisy, reasonable date could still be obtained. Similar results have been observed for other harmonics as well. We tend to focus on $n = 2$ if possible, since these signals have virtually no baseline curvatures or offsets (as seen in $n = 1$ spectra), and have higher signal levels than higher harmonic WMS spectra. We estimate that a precision of better than 25 torr is possible here.

The final method for determining pressure is based on the ratio of peak signal heights of different harmonic signals. Since the imaging array records the full modulated spectrum before demodulation, we can numerically obtain any and all of the harmonic spectra simultaneously. Computed results show that these peak ratios vary substantially with pressure, so as to potentially allow a high precision determination of the system pressure. Since all WMS harmonic peak heights scale linearly with concentration, their ratios are independent of the amount of gas present, so that they depend only on pressure. Figure 19 compares measured and computed data for a series of measurements for the 2:4 harmonic ratio. Note that the plot is logarithmic, so that for the range of pressure shown (50 – 760 torr), a typical ratio can vary by a factor of three or more. If one can measure the ratio to an absolute

value of 0.05, this corresponds to a precision of 2% in pressure. For different modulation depths (β) we see that the data follow the predicted curves quite well.

For both of these latter pressure determination methods, it is apparent that the simple theory is fairly good at matching the experimental observations, but it does not include secondary effects such as harmonic distortion, residual amplitude modulation, laser non-linearities, threshold and multi-mode effects, and contributions to the spectra from adjacent lines. Therefore, we believe that more accurate determination of pressure can be found by parameterizing the experimental data (at a specified modulation depth), such as with a second order polynomial, and then using this curve to predict the pressure from a measurement. With this approach, non-idealities of the actual laser sensor system are accounted for.

We tested the latter two approaches by measuring spectra in a "blind" experiment. One staff member made a set of measurements at different pressures while a second analyzed the data, not knowing the pressures. Results consistently showed that harmonic ratios of peak-peak signals produced the best results with standard deviation of ±15 torr over the range of 55 to 760 torr. The trough spacing method exhibited larger standard deviation of ±30 torr. In summary, both the trough-trough spacing and harmonic peak ratio methods show great promise for determination of pressure using the nascent WMS absorption spectra used to determine gas concentration, without the need for additional (time-consuming) measurements.

IV. Conclusion

The gas imaging system provided excellent data bandwidth (48 kHz per element), dynamic range (>100 dB at 96 kHz A/D sampling rate), saturation optical power (7.5 μW), and minimum detectable optical power (110 pW). The custom signal processing electronics performed very well. Measurements of water vapor and oxygen were conducted in ambient air, a diffusion flame burner, and a laboratory furnace. Due to the high-sensitivity of the device, time-averaging of the spectra were not needed. Using all 76 elements of the silicon linear array detector, an effective measurement bandwidth of 340 Hz was obtained, limited only by the system data bandwidth of 48 kHz. Certainly, using fewer points per laser scan or a reduced number of detector elements will increase the effective measurement bandwidth. Temperature measurements were conducted using a furnace at temperatures ranging from 300 to 800 K. Temperatures were calculated from peak ratios of 2*f* spectra and are accurate to ±25 K. Pressure measurements were conducted using a gas cell at pressures ranging from 25 to 760 torr. Pressures were calculated using four techniques. Approach using the harmonic ratio of peak height measurements showed the best results with standard deviation of ±15 torr.

The imaging sensor will be versatile with the capability to obtain spatial and temporal maps of flow properties at multiple physical locations along a test article. The imaging sensor will provide a suitable and compact platform for measurements in ground-based facilities and in-flight. Experimental data are crucial for validating current CFD models, and for developing new models for achieving high-fidelity simulations that are important to the engine designers. Moreover, this non-intrusive diagnostic tool could be used to probe inflow distortions in wind tunnels and engine inlets, and to assess performance of wall cavities as flameholders in scramjet engines.

Acknowledgments

This material is based upon work supported by the United States Air Force under Contract No. FA8650-07-M-2751.

References

[1]Gruber, M. R., Hagenmaier, M. A. and Mathur, T., AIAA Paper 2006-4680, 42nd AIAA/ASME/SAE/ASEE Joint Propulsion Conference & Exhibit (2006).Vatistas, G. H., Lin, S., and Kwok, C. K., *AIAA Journal*, Vol. 24, No. 11, 1986, pp. 1872, 1873.

[2]Liu, J., Tam, C.-J., Lu, T. and Law, C. K., AIAA Paper 2006-4862, 42ndAIAA/ASME/SAE/ASEE Joint Propulsion Conference & Exhibit (2006).

[3]Thakur, A. and Segal, C., AIAA Paper 2004-3831, 40th AIAA/ASME/SAE/ASEE Joint Propulsion Conference & Exhibit (2004).

[4]Edens, S. G., King, P. I., Gruber, M. R. and Hsu, K.-Y., AIAA Paper 2006-4861, 42nd AIAA/ASME/SAE/ASEE Joint Propulsion Conference & Exhibit (2006).

[5]Grossman, P., Maddalena, L. and Schetz, J.A., AIAA Paper 2006-4682, 42nd AIAA/ASME/SAE/ASEE Joint Propulsion Conference & Exhibit (2006).

[6]Yariv, A., Introduction to Optical Electronics (Holt, Reinhart, and Winston, Inc., N.Y., 1971).

[7]Rothman, L. S., Jacquemart, D., et al., J.Quant. Specrosc. Radiat. Trans. 92, 139-204 (2005).

[8]Silver, J. A. Appl. Opt. 1992, 31, 707-717.

[9]Bomse, D. S.; Stanton, A. C.; Silver, J. A., Appl. Opt. 31, 718-731 (1992).
[10]Stanton, A. C., et al., Proc. SPIE 2834, 41 (1996).
[11]Silver, J.A. and Hovde, D.C., 65, 1691-1694 (1994).
[12]Hovde, D.C., et al., J. Atmos. Chem. 20, 141 (1995).
[13]Cattaneo, H. and Hernberg, R., Appl. Opt. 44, 6593-6598 (2005).
[14]Liu, J.T.C., Jeffries J.B., and Hanson, R.K., Appl. Phys. B 78, 503–511 (2004).
[15]Silver, J. A.; Kane, D. J., Measurement Sci Technol. 10, 845 (1999).
[16]Goldstein, N., et al., Appl. Opt. 31, 3409-3415 (1992).
[17]Bomse, D.S. and Silver, J.A., U. S. Patent 6,356,350, issued March, 2002.